Fabrication and characterization of large numerical aperture, high-resolution optical fiber bundles based on high-contrast pairs of soft glasses for fluorescence imaging

B. Morova,[1] N. Bavili,[1] O. Yaman,[1] B. Yigit,[2] M. Zeybel,[2] M. Aydin,[3] B. Dogan,[4] R. Kasztelanic,[5] D. Pysz,[5] R. Buczynski,[5,6,8] and A. Kiraz[1,7,9]

[1]*Department of Physics, Koç University, 34450 Sariyer, Istanbul, Turkey*
[2] *Department of Gastroenterology and Hepatology, School of Medicine, Koç University, 34450 Sariyer, Istanbul, Turkey*
[3]*Department of Computer Engineering, Fatih Sultan Mehmet Vakif University, 34445 Beyoglu, Istanbul, Turkey*
[4]*Department of Computer Engineering, Marmara University, 34730 Kadikoy, Istanbul, Turkey*
[5]*Department of Glass, Institute of Electronic Materials Technology, Wolczynska 133, 01-919 Warsaw, Poland*
[6]*Faculty of Physics, University of Warsaw, Pasteura 5, 02-093 Warsaw, Poland*
[7]*Department of Electrical and Electronics Engineering, Koç University, 34450 Sariyer, Istanbul, Turkey*
[8]*ryszard.buczynski@fuw.edu.pl*
[9]*akiraz@ku.edu.tr*

Abstract: Fabrication and characterization of flexible optical fiber bundles (FBs) with in-house synthesized high-index and low-index thermally matched glasses are presented. The FBs composed of around 15000 single-core fibers with pixel sizes between 1.1 and 10 μm are fabricated using the stack-and-draw technique from sets of thermally matched zirconium-silicate ZR3, borosilicate SK222, sodium-silicate K209, and F2 glasses. With high refractive index contrast pair of glasses ZR3/SK222 and K209/F2, FBs with numerical apertures (NAs) of 0.53 and 0.59 are obtained, respectively. Among the studied glass materials, ZR3, SK222, and K209 are in-house synthesized, while F2 is commercially acquired. Seven different FBs with varying pixel sizes and bundle diameters are characterized. Brightfield imaging of a micro-ruler and a *Convallaria majalis* sample and fluorescence imaging of a dye-stained paper tissue and a cirrhotic mice liver tissue are demonstrated using these FBs, demonstrating their good potential for microendoscopic imaging. Brightfield and fluorescence imaging performance of the studied FBs are compared. For both sets of glass compositions, good imaging performance is observed for FBs, with core diameter and core-to-core distance values larger than 1.6 μm and 2.3 μm, respectively. FBs fabricated with K209/F2 glass pairs revealed better performance in fluorescence imaging due to their higher NA of 0.59.

1. Introduction

Fluorescence optical imaging is a powerful tool in biology and medical science. It enables labelling targeted structures and distinguishing them unambiguously from the host while collecting functional and spatial information on biological tissues, cells and subcellular structures. However, due to limited penetration of light into a biological tissue, non-invasive *in vivo* imaging is extremely difficult with conventional, high-resolution fluorescence microscopes. To overcome this limitation, fiber-based fluorescence microscopy systems have been designed. Fluorescence micro-endoscopy (FME) [1,2], fiber-optic confocal microscopy [3–9], two-photon FME [2,10–15] are some of those fiber-optic fluorescence imaging

modalities. For all these techniques, optical fibers provide reduction in the size of the microscope and a flexible microscope probe for delivery of the excitation light. However, regular single mode fibers (SMFs) have limited ability for efficient excitation delivery and signal collection. Many of the limitations of single-mode optical fibers in endoscopic imaging can be circumvented by using multimode optical fibers (MMFs) [16–19]. When a light wave couples to single-core MMF, numerous spatial modes can be transported, and these modes can be used for imaging purposes. For that, wave distortion arising from mode dispersion should be handled [20]. Several ways were proposed to overcome this distortion problem. Čižmár et al. developed a wave-front shaping technique that enables transmission imaging using single-core MMF [19]. Also, Choi et al. eliminated distortion by employing the speckle imaging method and demonstrated wide-field endoscopic imaging [18]. However, in these methods, transmission matrix calculation, image reconstruction processes or/and scanning mechanism at distal end of the fiber [12,21–23] are required to obtain transmission or fluorescence images. In addition, single-core MMF based systems are highly sensitive to bending or twisting due to the variations in the transmission matrix.

The use of FBs which consist of thousands of cores within a single element of sub-millimeter diameter, attract much attention especially due to their potential in micro-endoscopic *in-vivo* imaging applications. FBs provide direct image transmission where each individual fiber core serves as a single imaging pixel. Also, the transported image is not affected by distortions caused by bending or twisting of the optical fiber as long as intercore coupling do not degrade the transferred image. Hence, FBs offer fully flexible imaging probes. FBs can be used for imaging without the requirement of a scanning mechanism at the distal end of the fiber [24,25], and they can be incorporated in more sophisticated imaging systems that use confocal [24,26,27] or structured light illumination approaches [28–30]. Several recent microscopic imaging demonstrations using FBs include: deep-brain imaging of a living animal [31], *in vivo* subcellular resolution imaging of cancerous tissues such as oral, cervical and ovarian [32–35], *ex-vivo* human stomach, animal colon, liver and belly tissue imaging [36], and thermal infrared imaging [37–40]. Currently best FBs dedicated for fluorescent imaging have pixel sizes larger than 3 μm and NA values smaller than 0.40 [31,41].

Besides its advantages described in the previous paragraph, FB fluorescence imaging comes together with critical restrictions on resolution and contrast. First of all, commercial FBs are manufactured by a limited variety of commercially available glasses, limiting the NA values of FBs at around 0.56 [42]. Higher NA values are critical for reducing the optical crosstalk between the fibers, and hence improving the overall imaging performance. This is especially important for the case of fluorescence imaging. Fluorescence emission obtained from excitation of tissues has a Lambertian profile of emission and limited intensity to avoid overheating of the tissues. Therefore, large NA of FB is highly demanded to transfer measurable signal via the FB without crosstalk. Also, pixelation is a fundamental artifact in FB-based imaging caused by the core-to-core distance between individual fibers. This distance can be reduced only down to a certain limit because thin cladding layers also result in larger optical crosstalk between adjacent fiber cores [12]. Although different approaches such as low-pass filtering [43], mechanical and spectral shifting [36,44], wavefront shaping [45] or image registration-based compounding [46] have been presented in order to eliminate pixelation artifacts, post-processing of images is often needed. Besides, a scanning system may also be employed at the proximal end of the FB in order to improve the image quality. In addition to all these, the use of alternative materials for manufacturing FBs to overcome such restrictions is needed. In order to increase the FB resolution, reduction of pixel size is required, while maintaining a low optical crosstalk between neighboring pixels especially in the presence of bending. Specialized FBs fabricated using high contrast pairs of glasses promise to fulfil these requirements. Further decrease of pixel size was demonstrated when

thermally matched soft glasses with refractive index difference of 0.37 were used for FB development [47].

In this work, we report the fabrication and characterization of flexible, lensless and high-resolution imaging FBs with a variety of pixel size and field of view using novel in-house synthesized zirconium, sodium and borosilicate soft glasses. Stack-and-draw technique was used to fabricate FBs with approximately 15000 pixels ordered in a hexagonal lattice based on in-house synthesized glasses. Use of in-house synthesized soft glasses allows us to obtain relatively high refractive index contrast between the fiber core and cladding compared to commercially available FBs made with silica glasses [42,48,49]. Our FBs had NA values of 0.53 or 0.59. These high NA FBs bring together increased fluorescence collection efficiencies and reduced mode overlaps between neighboring fiber cores, i.e. reduced optical crosstalk. These imply better imaging contrast especially for fluorescence applications. We performed numerical analysis which verify the effects of the NA and FB geometry to fluorescence collection efficiency and mode overlap. Increasing the NA of the FBs also allows for reducing the core-to-core distances without a significant reduction in image contrast, resulting in less pixelation artifacts [50]. Critical FB parameters such as core size, pitch between the individual fibers, and NA of fibers were verified so as to optimize the imaging quality. The brightfield and fluorescence imaging properties of these bundles were characterized. First, wide-field imaging experiments on both transmission and fluorescence of a micro-ruler sample, *Convallaria majalis* sample and dye stained paper tissue sample were carried out and the pixel size effects on resolution were compared. Afterwards, *ex-vivo* fluorescence imaging of a cirrhotic mice liver tissue that is cleared using the CLARITY technique [51] was performed, and the resulting image contrasts were compared. We also performed fluorescence imaging experiments with FBs in presence of several bending radii as small as 32 mm and observed good contrast for all cases. Our results show significant improvements on FB development with novel material systems for non-invasive, fast and high-resolution fluorescence imaging. Such flexible, high NA FBs can enhance the contrast of the collected fluorescence images thanks to their relatively large collection efficiencies and small mode overlaps.

2. Development of imaging fiber bundles

Optical FBs studied in this work are fabricated using two different pairs of glass materials [47–49]. The first set includes in-house synthesized high-index zirconium-silicate glass labelled ZR3 (40.5% SiO_2, 17.5% ZrO_2, 12.0% BaO, 12.0% Na_2O, 10.0% B_2O_3, 5.0% CaO and 3.0% K_2O) and in-house synthesized low-index borosilicate glass labelled SK222 (68.4% SiO_2, 12.3% Na_2O, 7.1% CaO, 7.1% ZnO, 2.4% Al_2O_3, 2.0% B_2O_3 and 0.7% K_2O). The second set includes in-house synthesized high-index sodium-silicate glass labelled K209 (49.88% SiO_2, 31.4% B_2O_3, 9.67% Na_2O, 7.09% K_2O and 1.96% Al_2O_3) and commercially available low-index lead-silicate F2 glass (45.7% SiO_2, 45.5% PbO, 5.0% K_2O, 3.5% Na_2O and 0.8% As_2O_3). Each pair of glasses are thermally matched which ensures that they can be drawn together on the optical tower. The basis optical and thermo-physical parameters of the glasses are presented on Table 1.

To develop the FB elements, the modified standard technique for fabricating the step-index fibers is used [52]. The technique consists of several steps shown in Fig. 1. First, a circular rod, approximately 10 mm in diameter, made from high-index glass and a tube with an internal diameter of 10 mm and an outer diameter of about 20 mm made from low-index glass are prepared. Next, after inserting the rod into the tube, both glasses are drawn on the optical fiber drawing tower and scaled down to obtain a rod with a diameter of about 400 µm. Then, approximately 15000 rods produced in this way are inserted into a thin-walled capillary made of low-index glass to form final preform. The rods form a hexagonal structure where each rod performs the role of a single 'pixel' in the optical bundle. Finally, the FB preform is drawn on the optical fiber drawing tower and scaled down to obtain the final optical bundle.

This approach enables obtaining FBs with varying diameters and pitch between each 'pixel' from the same preform. Furthermore, it ensures that the individual 'pixels' in a particular FB have precisely the same optical properties.

Table 1. Optical and thermo-physical parameters of the glasses: n_d – refraction index (d-line), α – linear thermal expansion (20 ÷ 450°C range), DTM – dilatometric softening point, T_g – transition temperature, T_z – ovalization point, T_k – sphere point, T_{pk} – hemisphere point.

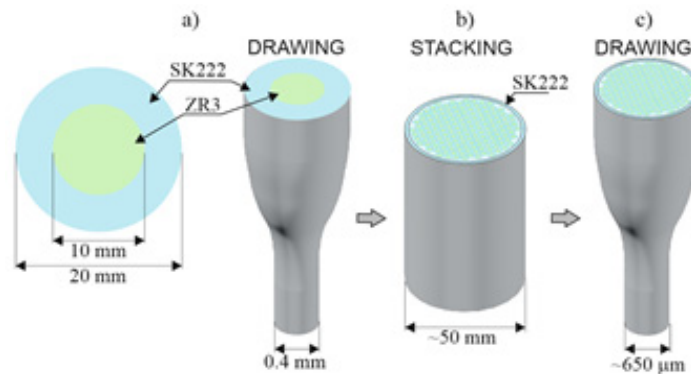| Parameters	Glass Symbol			
	SK222	ZR3	K209	F2
n_d	1.520	1.609	1.508	1.619
α [10^{-7} K^{-1}]	89.0	94.5	93.0	93.0
DTM [°C]	610	644	527	93.0
Temp [°C]				
T_g $\log \eta = 13.4$	542	581	492	431
T_z $\log \eta = 9.0$	700	680	590	520
T_k $\log \eta = 6.0$	820	790	690	690
T_{nk} $\log \eta = 4.0$	950	865	765	820

Fig. 1. Schematic of stack-and-draw process for optical FB fabrication: (a) Development of individual rods made of two types of thermally matched glasses, (b) assembly of perform, (c) drawing final fiber optic bundle.

3. Characterization of fiber bundles

FBs were prepared and characterized in two different groups consisting of three and four FB samples respectively, all having approximately the same number of individual fibers (~15000). The lead-free Zr3/SK222 glasses are used as core and cladding materials in the fabrication of the first group with pixel sizes of 1.1 μm, 1.6 μm, and 10 μm. In the second group of FBs, in-house synthesized K209 and commercially available lead-silicate F2 glass are used as core and cladding materials. Second group consist of FBs with pixel sizes of 1.9 μm, 2.4 μm, 2.5 μm, and 2.9 μm. Scanning electron microscope (SEM) images of the cross sections of these bundles are presented in Fig. 2, and main specifications of fabricated FBs are given in Table 2. The missing pixels in some of the imaging bundles presented in Fig. 2, are the result of defects in the hexagonal lattice assembly that occurred at the stage of fabrication of the image bundles. However, the number of defects is very small and does not exceed 0.5% for all FBs. Therefore, their influence on image quality is very limited.
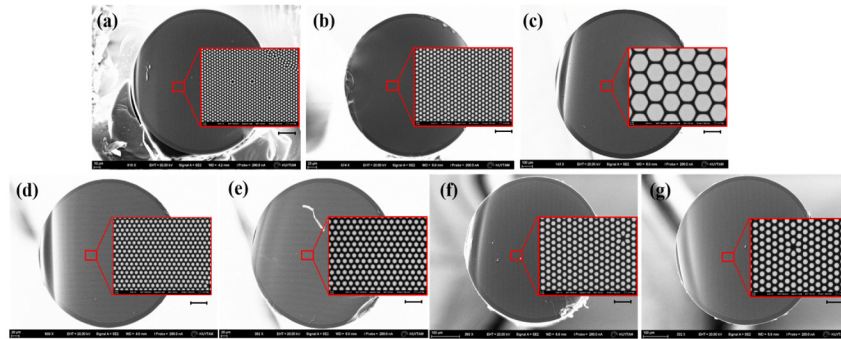
Fig. 2. SEM images of FB 1-7 with core sizes of (a) 1.1 μm, (b) 1.6 μm, (c) 10 μm, (d) 1.9 μm, (e) 2.4 μm, (f) 2.5 μm, and (g) 2.9 μm, respectively. Enlarged images inside the red boxes were taken with a 5000X magnification. Scale bars under the enlarged images represent 10 μm length.

First group of FBs (FB 1-3) has core refractive index (n_f) and cladding refractive index (n_c) of 1.609 and 1.520, respectively measured for sodium D-line. For the second group of FBs (FB 4-7) n_f and n_c are measured to be 1.619 and 1.508, respectively. As we discuss in the following, due to higher refractive index contrast (n_f/n_c), the optical cross talk between adjacent fiber cores is lower for the second group, which results in better overall imaging performance.

For each FB, the total diameter which corresponds to the imaged field-of-view, and the measured numerical aperture (NA) values are also given in Table 2. NA of an individual fiber inside a FB describes its light-gathering ability. For NA measurements, both ends of FBs were first cleaved with a 20 mm length. After that, the laser beam (488 nm wavelength) was focused at the proximal end of a FB using a microscope objective (Nikon L Plan SLWD, 50x, NA = 0.45), and transmitted laser beam widths at known distances from the FB's other end were measured by a CMOS camera (Thorlabs, DCC1545M). The use of a high magnification microscope objective enables coupling the laser beam to only a few fibers in a FB, which is required for precise NA measurement of individual fibers. As an example, full width half maximum (FWHM) of the beam as a function of distance from the bundle tip measured relative to the first measurement point is given in Fig. 3 for the FB 7. From the linear fit, the NA of the FB 7 is calculated as 0.59 which is in good agreement with the theoretical predictions. The NA measurements were performed for all FBs in the same way, and the measured NA values are given in Table 2. Measured values are consistent for each group of FBs and they are in general agreement with the theoretical predictions given by $NA = \sqrt{n_f^2 - n_c^2}$ that reveals 0.53 and 0.59 for FBs 1-3 and 4-7, respectively. Slight variations between the measured and calculated NA values are attributed to uncertainties caused by coupling of the laser beam to multiple fibers during the measurements. For each FB, the minimum bending radius was also characterized. Approximate minimum bending radii were determined by measuring the radius of curvatures of the FBs after the FB was angled 90° without excessive bending. These measured values are also given in Table 2.
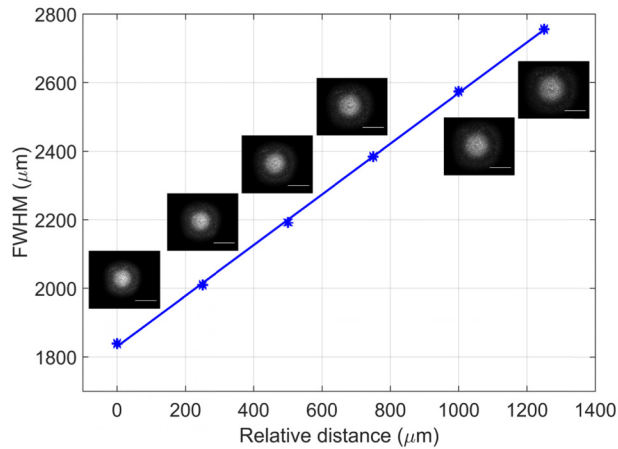
Fig. 3. Measured FWHMs of the beam as a function of distance from bundle tip. Insets show the 2D intensity profiles of the beam at given positions for the FB7. The square roots of the 2D data are shown in the insets for clarity. Scale bars on the 2D intensity profiles indicate 2 mm length.

Table 2. Specifications of developed imaging FBs.

Specifications	FB 1	FB 2	FB 3	FB 4	FB 5	FB 6	FB 7
Glass types (core/cladding)	ZR3/SK222	ZR3/SK222	ZR3/SK222	K209/F2	K209/F2	K209/F2	K209/F2
n_f/n_c	1.058	1.058	1.058	1.074	1.074	1.074	1.074
Total diameter (mm)	0.23	0.32	1.35	0.38	0.49	0.50	0.58
Core diameter (µm)	1.1	1.6	10	1.9	2.4	2.5	2.9
Core-to-core distance (µm)	1.6	2.3	11.2	2.7	3.5	3.7	4.2
Measured NA	0.53	0.52	0.55	0.60	0.62	0.58	0.59
Bending radius (mm)	22	28	rigid	32	65	110	75

A numerical analysis was also carried out to study how the efficiency of light collection depends on the NA of the presented fibers in comparison with fibers with a smaller NA [53]. The collection efficiency, η, for a single core, that represents a single pixel in the FB located in a medium with refractive index n_0 and collecting light from planar fluorescent source with area A_s, is given as [54,55]:

$$\eta = \frac{NA^2}{2n_0^2} \frac{\pi d^2}{4A_s},$$ (1)

where d denotes the core diameter, NA is the numerical aperture, and A_s is a function of the distance z between the fluorescent plane and the fiber surface:

$$A_s = \frac{\pi d^2}{4}\left(1 + \frac{2NAz}{dn_0}\right)^2.$$ (2)

Figure 4(a) presents η values calculated for FBs with various d and NA values. This relationship shows that, for a constant core diameter, the collection efficiency increases with increasing NA. Therefore, in order to achieve the highest possible resolution and at the same time the highest possible collection efficiency in fluorescence imaging, it is necessary to increase the NA.
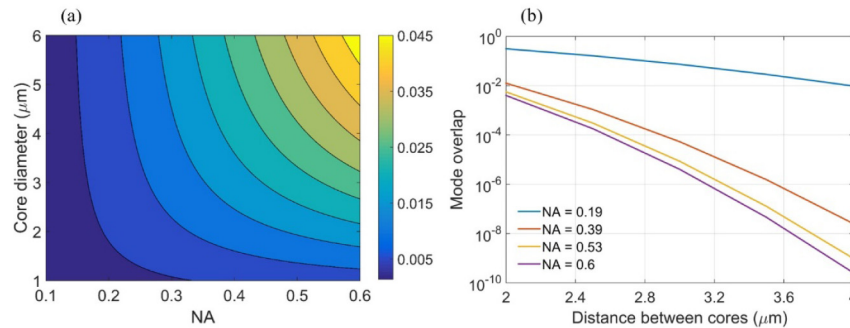
Fig. 4. Influence of NA on optical FB performance: a) Dependence of the collection efficiency, η, on fiber core diameter, d, and NA, b) dependence of the mode overlap integral on the distance between centers of the cores for pair of cores with the diameter of 2 µm each and various NA values.

NA also influences the optical crosstalk between the neighbouring pixels and consequently the transferred image contrast and quality. The coupling between cores in the FB is determined by the overlap of the electric field distributions of their guided modes. This task can be limited to the analysis of two neighbouring cores and calculation of overlap integral f between their complex electrical fields [56]:

$$f = \frac{\left| \int E_1^* E_2 \, dA \right|^2}{\int |E_1|^2 \, dA \int |E_2|^2 \, dA},$$

(3)

where E_1 and E_2 represent the complex electric field functions of the guided modes in the first and second core, respectively.

We have used the finite element method (COMSOL Multiphysics) to calculate the overlap integral for FBs with fixed core diameter of 2 µm and different NA values as a function of the distance between the centers of the cores. We show that, for every particular distance between the cores, the mode overlap significantly decreases with an increase in NA (Fig. 4(b)). Hence, we conclude that FBs with high NA values provide low optical crosstalk even for relatively small distances between the neighbouring cores. High NA is obtained when refractive index difference between the core and cladding is increased. Simultaneously it allows for better confinement of the mode in the core area and reduction of the distance between neighbouring cores in the FB, resulting in less pixelation artifacts.

4. Brightfield and fluorescent imaging with fiber bundles

The experimental setup used for brightfield and fluorescence imaging with FBs is presented in Fig. 5. A direct contact between the imaging bundle and imaged sample was employed in all of our experiments except for those in which the *Convallaria majalis* sample was imaged. Since the *Convallaria majalis* sample was located beneath a cover glass, the proximal end of the FB could not be placed immediately in contact with that sample. Only for this sample, an imaging doublet pair was employed between the proximal end of the FB and the sample for collecting the brightfield images. In the experimental setup, there are two different illumination modules for brightfield transmission and epifluorescence imaging systems. For transmission, a standard broadband light source was used to illuminate the sample that was placed between the light source and the distal end of the FB. Hence, transmitted light is transferred to the FB directly. For fluorescence imaging, an Ar + ion laser with a central wavelength of 488 nm was used to excite the samples. The incident laser light passed through a spherical plan-convex lens (f = 100 mm) and reflected from a dichroic mirror to a focusing objective with 50x magnification (Nikon L Plan SLWD). Here, the convex lens was used to

focus the laser beam into the back-focal plane of the objective and, thus, to establish for wide-field illumination of the fiber bundle. The proximal end of the FB was placed in the front-focal plane of the microscope objective. Hence, excitation light was transferred to the sample through the FB itself. For detection, both brightfield and fluorescence imaging systems used the same imaging module. FB collected the transmitted or emitted fluorescence light and transferred it to the microscope objective. After the microscope objective, the light passed through the dichroic mirror and two longpass filters (Thorlabs, FEL0500 and FGL495) which blocked the excitation wavelength. Afterwards, an achromatic doublet lens (f = 50 mm) that served as the tube lens of the infinity-corrected imaging system transferred the transmitted or emitted light to a CMOS camera (Hayear, HY-3307). A micrometer translation stage was used to control the position of the sample relative to the fiber bundle. Brightfield microscopy experiments were performed with two samples: A micro-ruler sample and a *Convallaria majalis* (Lily of the Valley) root tissue [57] sample. While, fluorescence imaging experiments employed a lens cleaning paper tissue sample stained with fluorescein dye and cirrhotic liver tissues stained with fluorescein isothiocyanate (FITC). We note that photobleaching did not hamper our fluorescence imaging experiments due to the use of high fluorophore concentrations together with low laser intensities and low laser exposure times.

The fluorescence images shown in this manuscript were recorded from different positions on the samples and employed different laser intensities and camera parameters optimizing the image contrast. Hence, intensities in the reported fluorescence images do not represent a direct measure for the fluorescence collection efficiencies of individual FBs. We also recorded fluorescence images of similar locations in the dye-stained paper tissue sample with FBs 2 and 4 using the same laser excitation power and camera parameters. In agreement with the theoretical predictions, these images showed larger collected fluorescence intensities with FB 4 in contrast to FB 2. We refrained ourselves from making a quantitative comparison between these results and the theoretical predictions shown in Fig. 4(a), mainly because of sample deformations between measurements upon contact with the FB, and FB coupling efficiency variations caused by fiber cleaving.
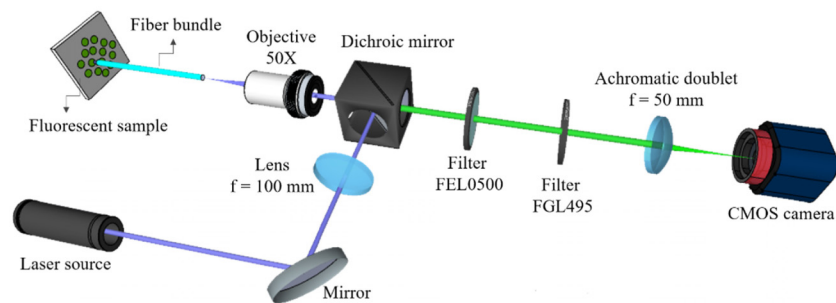

Fig. 5. Schematics of the setup used for fluorescence imaging experiments using fiber bundles.

Figures 6(a)–(c) and 6(d)–(f) show brightfield images of the micro-ruler, and *Convallaria majalis* samples acquired with broadband light source by FBs 1-3 whose pixel sizes are 1.1 μm, 1.6 μm, and 10 μm. The quality of the brightfield image acquired by FB 1 is lower in comparison with the images acquired using FBs 2 and 3. Figures 6(g)–(i) present fluorescence images of the dye stained paper tissue sample acquired by FBs 1-3, respectively. Fluorescence emitted from the fibers of the paper tissue is apparent in all images. For FBs 1 and 2 with small pixel size, the poor quality of the fluorescence images is attributed to optical crosstalk between individual fibers in a FB caused by a relatively low refractive index contrast between fiber core and fiber cladding (i.e. low NA).

The contrast of a brightfield or fluorescence image was quantified by σ/μ where σ is the standard deviation of pixel intensity and μ is the mean pixel intensity of a selected region of

interest in a given image. While σ increases with the contrast of an image, division by μ compensates for the changes in the overall brightness of different images. σ/μ values calculated for all brightfield and fluorescence images in this paper are shown in Table 3. In order to investigate imaging quality in the presence of bending, fluorescence images of stained paper tissue were recorded using FB 2 for several bending radii (infinity, 190 mm, 120 mm and 32 mm). The resulting σ/μ values were calculated in the range of $0.25 - 0.39$ which revealed a good contrast for all cases.

When the transmission and fluorescence images shown in Fig. 6 are compared, we observe that image resolution and contrast are comparatively lower for the case of fluorescence imaging with FBs 1 and 2. In case of transmission imaging, created image is only based on scattering and absorption of the illumination light. Therefore, the properties of an image are defined by illumination conditions. In case of fluorescence imaging, image is created as re-emission from fluorescent dyes and properties of the image are defined by the Lambertian emission. As a result, for low NA FBs, it is not possible to collect all the emitted light into respective pixels. Some fluorescence emitted with relatively larger divergence angles leaks into neighboring fibers creating a bright background in the image, hence reducing the image quality [41].

Figures 7(a)–(d) and 7(e)–(h) show brightfield images of the micro ruler and *Convallaria majalis* samples recorded using FBs 4-7 whose pixel sizes are 1.9 µm 2.4 µm, 2.5 µm, and 2.9 µm. Fluorescence images of the dye stained paper tissue sample are also shown in Figs. 7(i)–(l). Good image contrasts are observed in all the brightfield and fluorescence images shown in Fig. 7. Hence significant improvements on transmission and fluorescence images are observed with FBs 4-7 thanks the relatively high NA of these FBs in comparison with FBs 1-3.
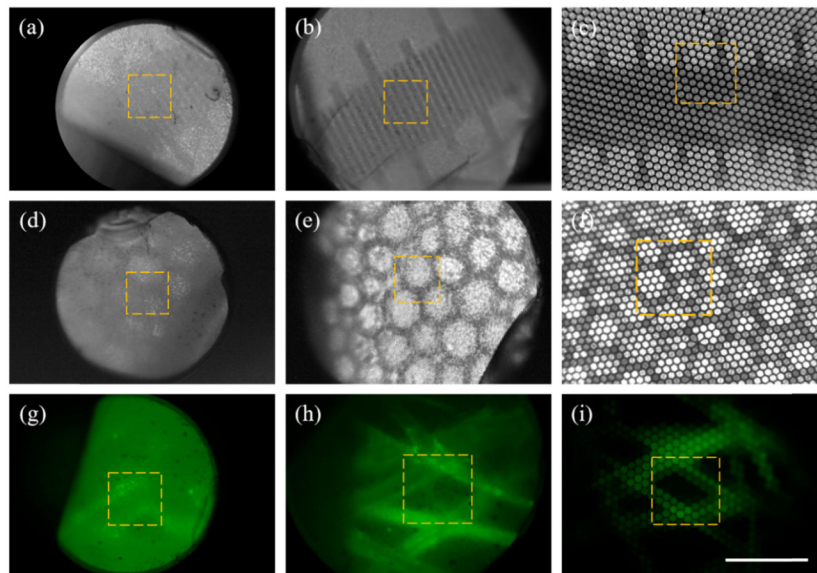

Fig. 6. Brightfield images of the micro-ruler sample (a-c), brightfield images of the *Convallaria majalis* sample (d-f), and fluorescence images of the fluorescein stained paper tissue sample (g-i) as-recorded by FBs 1-3, respectively. Scale bar: 100 µm. Dashed boxes indicate the regions used for σ/μ calculations.
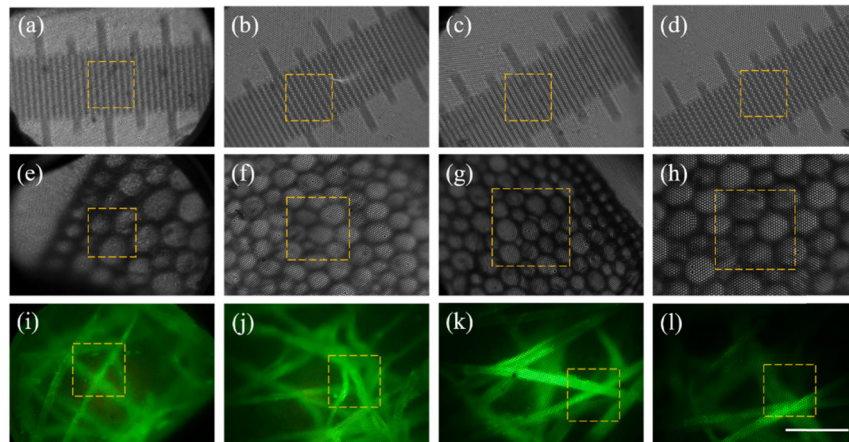
Fig. 7. Brightfield images of the micro-ruler sample (a-d), brightfield images of the *Convallaria majalis* sample (e-h), and fluorescence images of the fluorescein stained paper tissue sample (l-l) as-recorded by FBs 4-7, respectively. Scale bar: 100 μm. Dashed boxes indicate the regions used for σ/μ calculations.

Table 3. σ/μ values calculated for the regions indicated with dashed boxes in different images in Figs. 6, 7, and 8.

	FB 1	FB 2	FB 3	FB 4	FB 5	FB 6	FB 7
Brightfield images of micro-ruler	0.18	0.11	0.38	0.43	0.33	0.33	0.30
Brightfield images of *Convallaria majalis*	0.23	0.32	0.47	0.38	0.35	0.54	0.58
Fluorescence images of paper tissue	0.09	0.27	0.65	0.30	0.28	0.52	0.89
Fluorescence images of liver tissue	0.07	0.27	0.27	0.18	0.35	0.38	0.48

In order to demonstrate the micro-endoscopic imaging capability of the studied FBs, *ex-vivo* imaging of cirrhotic mice liver stained with FITC was performed. Before staining, the liver tissue was cleared by using the method of CLARITY following the sample preparation protocol described in Ref [51]. This method helps to stabilize the tissue structure by preserving protein and nucleic acid contents of the sample via acrylamide-based monomers. In order to obtain a transparent sample, thermal lipid removal steps were applied by sodium borate buffer (200 mM, pH 8.5) containing 4% (wt/vol) sodium dodecyl sulfate (SDS) for 2-3 weeks. After this clearing process, optically cleared biological sample was labelled with 1:100 α-smooth muscle actin - FITC antibody (Sigma Aldrich, F3777). We note that this clearing process is not necessary for collecting the fluorescence signal from biological tissues in contact imaging mode with FBs. Such a tissue clearing approach will be especially important for noncontact fluorescence imaging of the samples with FBs. FITC has a peak absorption of 488 nm and peak emission of 515 nm thus, an argon ion laser with 488 nm central wavelength was used for exciting the specimen. With the FB tip placed in contact with the specimen at nodular cirrhotic area, cross-section of a vein and hepatocellular region are visible (especially in Figs. 8(b)–(g)). These structures in the nodular region are typical type of structure at the advanced stages of cirrhosis and liver disease.
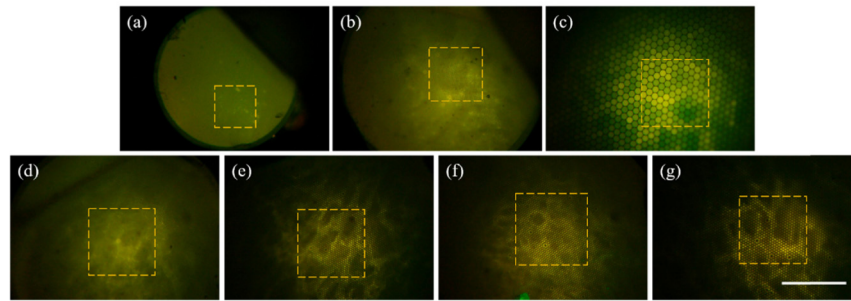
Fig. 8. As-recorded fluorescent images of the cirrhotic liver tissue sample using FB 1 (a), FB 2 (b), FB 3 (c), FB 4 (d), FB 5 (e), FB 6 (f), and FB 7 (g). Tissue was clarified using CLARITY method and stained with fluorescein (FITC). Excitation wavelength is 488 nm. Scale bar: 100 μm. Dashed boxes indicate the regions used for σ/μ calculations.

5. Conclusions

In this paper, we demonstrated fluorescence and transmission imaging performance results of FBs developed with two different sets of glass compositions: Lead-free zirconium-silicate and borosilicate glasses (ZR3/SK222), sodium-silicate and lead-silicate glasses (K209/F2). The considered pairs of glasses are thermally matched and offer high difference of refractive indices, 0.089 for ZR3/SK222, and 0.111 for K209/F2. As a result, high NA for both types of FBs are obtained: NA = 0.53 and NA = 0.59, respectively. Using stack-and-draw method, we produced FBs with approximately 15000 pixels ordered in a hexagonal lattice and various diameters, core sizes and distances between the pixels. We tested seven different FBs with core sizes varying between 1.1 and 10 μm. To study the effect of the NA and pixel size on their performance, we recorded brightfield images of a micro-ruler and a *Convallaria majalis* sample, and fluorescence images of a dye stained paper tissue and *ex-vivo* cirrhotic liver tissue. We also performed numerical studies to verify the effects of NA, core diameter and core-to-core distance to fluorescence collection efficiency and mode overlap between neighboring fiber cores. Results revealed good image resolution and contrast for all FBs except for FB 1 (Core diameter = 1.1 μm, core-to-core distance = 1.6 μm, and NA = 0.53) in cases of both transmission and fluorescence imaging. Minimum core diameter and core-to-core distance values of 1.6 μm and 2.3 μm were sufficient for eliminating the optical crosstalk between individual cores even in the presence of bending for both sets of glass compositions. FBs 2, 4-7 have pixel sizes similar to the ones previously reported by other groups (NA = 0.4; core diameter = 2.2 μm; core-to-core distance<4 μm in Ref [31], NA = 0.27; core diameter = 1.8 μm; core-to-core distance~3.5 μm in Ref [41]), but offer much larger NA. As a result, they can collect higher fluorescent signal and achieve higher contrast values especially in fluorescence imaging. For FBs with smaller pixel size (FB 4) or lower contrast of refractive index (FB 1, 2) images were relatively degenerated due to the cross-talk between individual pixels. In order to ensure high imaging quality with smaller pixel sizes, refractive index contrast (n_f/n_c) can be further increased for an optimum core-to-core distance reducing the cross-talk between neighboring pixels. Our results show the good potential of the studied high NA FBs fabricated using in-house synthesized soft glasses for micro-endoscopic fluorescence imaging applications.

Funding

Acknowledgments

References

1. J. A. N. Fisher, E. F. Civillico, D. Contreras, and A. G. Yodh, "In vivo fluorescence microscopy of neuronal activity in three dimensions by use of voltage-sensitive dyes," Opt. Lett. **29**(1), 71–73 (2004).
2. J. C. Jung, A. D. Mehta, E. Aksay, R. Stepnoski, and M. J. Schnitzer, "In Vivo Mammalian Brain Imaging Using One- and Two-Photon Fluorescence Microendoscopy," J. Neurophysiol. **92**(5), 3121–3133 (2004).
3. P. M. Delaney, M. R. Harris, and R. G. King, "Fiber-optic laser scanning confocal microscope suitable for fluorescence imaging," Appl. Opt. **33**(4), 573–577 (1994).
4. R. Kiesslich, J. Burg, M. Vieth, J. Gnaendiger, M. Enders, P. Delaney, A. Polglase, W. McLaren, D. Janell, S. Thomas, B. Nafe, P. R. Galle, and M. F. Neurath, "Confocal laser endoscopy for diagnosing intraepithelial neoplasias and colorectal cancer in vivo," Gastroenterology **127**(3), 706–713 (2004).
5. T. Ota, H. Fukuyama, Y. Ishihara, H. Tanaka, and T. Takamatsu, "In situ fluorescence imaging of organs through compact scanning head for confocal laser microscopy," J. Biomed. Opt. **10**(2), 024010 (2005).
6. G. D. Papworth, P. M. Delaney, L. J. Bussau, L. T. Vo, and R. G. King, "In vivo fibre optic confocal imaging of microvasculature and nerves in the rat vas deferens and colon," J. Anat. **192**(Pt 4), 489–495 (1998).
7. W. Piyawattanametha, H. Ra, Z. Qiu, S. Friedland, J. T. Liu, K. Loewke, G. S. Kino, O. Solgaard, T. D. Wang, M. J. Mandella, and C. H. Contag, "In vivo near-infrared dual-axis confocal microendoscopy in the human lower gastrointestinal tract," J. Biomed. Opt. **17**(2), 021102 (2012).
8. H.-J. Shin, M. C. Pierce, D. Lee, H. Ra, O. Solgaard, and R. Richards-Kortum, "Fiber-optic confocal microscope using a MEMS scanner and miniature objective lens," Opt. Express **15**(15), 9113–9122 (2007).
9. L. D. Swindle, S. G. Thomas, M. Freeman, and P. M. Delaney, "View of Normal Human Skin In Vivo as Observed Using Fluorescent Fiber-Optic Confocal Microscopic Imaging," J. Invest. Dermatol. **121**(4), 706–712 (2003).
10. D. Bird and M. Gu, "Two-photon fluorescence endoscopy with a micro-optic scanning head," Opt. Lett. **28**(17), 1552–1554 (2003).
11. C. J. Engelbrecht, R. S. Johnston, E. J. Seibel, and F. Helmchen, "Ultra-compact fiber-optic two-photon microscope for functional fluorescence imaging in vivo," Opt. Express **16**(8), 5556–5564 (2008).
12. B. A. Flusberg, J. C. Jung, E. D. Cocker, E. P. Anderson, and M. J. Schnitzer, "In vivo brain imaging using a portable 3.9 gram two-photon fluorescence microendoscope," Opt. Lett. **30**(17), 2272–2274 (2005).
13. F. Helmchen, M. S. Fee, D. W. Tank, and W. Denk, "A Miniature Head-Mounted Two-Photon Microscope. High-Resolution Brain Imaging in Freely Moving Animals," Neuron **31**(6), 903–912 (2001).
14. M. J. Levene, D. A. Dombeck, K. A. Kasischke, R. P. Molloy, and W. W. Webb, "In vivo multiphoton microscopy of deep brain tissue," J. Neurophysiol. **91**(4), 1908–1912 (2004).
15. D. R. Rivera, C. M. Brown, D. G. Ouzounov, W. W. Webb, and C. Xu, "Multifocal multiphoton endoscope," Opt. Lett. **37**(8), 1349–1351 (2012).
16. M. Plöschner, T. Tyc, and T. Čižmár, "Seeing through chaos in multimode fibres," Nat. Photonics **9**(8), 529–535 (2015).
17. I. N. Papadopoulos, S. Farahi, C. Moser, and D. Psaltis, "High-resolution, lensless endoscope based on digital scanning through a multimode optical fiber," Biomed. Opt. Express **4**(2), 260–270 (2013).
18. Y. Choi, C. Yoon, M. Kim, T. D. Yang, C. Fang-Yen, R. R. Dasari, K. J. Lee, and W. Choi, "Scanner-free and Wide-Field Endoscopic Imaging by Using a Single Multimode Optical Fiber," Phys. Rev. Lett. **109**(20), 203901 (2012).
19. T. Čižmár and K. Dholakia, "Exploiting multimode waveguides for pure fibre-based imaging," Nat. Commun. **3**(1), 1027 (2012).
20. M. C. T. Bahaa,and E. A. Saleh, *Fundamentals of Photonics,* 2nd ed. (John Wiley & Sons, New York, 2007).
21. G. Oh, E. Chung, and S. H. Yun, "Optical fibers for high-resolution in vivo microendoscopic fluorescence imaging," Opt. Fiber Technol. **19**(6), 760–771 (2013).
22. R. Barankov and J. Mertz, "High-throughput imaging of self-luminous objects through a single optical fibre," Nat. Commun. **5**(1), 5581 (2014).
23. S. M. Kolenderska, O. Katz, M. Fink, and S. Gigan, "Scanning-free imaging through a single fiber by random spatio-spectral encoding," Opt. Lett. **40**(4), 534–537 (2015).
24. A. F. Gmitro and D. Aziz, "Confocal microscopy through a fiber-optic imaging bundle," Opt. Lett. **18**(8), 565–567 (1993).
25. R. Juškaittis, T. Wilson, and T. F. Watson, "Real-time white light reflection confocal microscopy using a fibre-optic bundle," Scanning **19**(1), 15–19 (1997).
26. J. Knittel, L. Schnieder, G. Buess, B. Messerschmidt, and T. Possner, "Endoscope-compatible confocal microscope using a gradient index-lens system," Opt. Commun. **188**(5-6), 267–273 (2001).
27. P. M. Lane, A. L. P. Dlugan, R. Richards-Kortum, and C. E. Macaulay, "Fiber-optic confocal microscopy using a spatial light modulator," Opt. Lett. **25**(24), 1780–1782 (2000).

28. N. Bozinovic, C. Ventalon, T. Ford, and J. Mertz, "Fluorescence endomicroscopy with structured illumination," Opt. Express **16**(11), 8016–8025 (2008).

29. M. Kyrish, J. Dobbs, S. Jain, X. Wang, D. Yu, R. Richards-Kortum, and T. S. Tkaczyk, "Needle-based fluorescence endomicroscopy via structured illumination with a plastic, achromatic objective," J. Biomed. Opt. **18**(9), 096003 (2013).

30. A. Shinde, S. M. Perinchery, and V. M. Murukeshan, "A targeted illumination optical fiber probe for high resolution fluorescence imaging and optical switching," Sci. Rep. **7**(1), 45654 (2017).

31. M. Kim, J. Hong, J. Kim, and H. J. Shin, "Fiber bundle-based integrated platform for wide-field fluorescence imaging and patterned optical stimulation for modulation of vasoconstriction in the deep brain of a living animal," Biomed. Opt. Express **8**(6), 2781–2795 (2017).

32. T. J. Muldoon, M. C. Pierce, D. L. Nida, M. D. Williams, A. Gillenwater, and R. Richards-Kortum, "Subcellular-resolution molecular imaging within living tissue by fiber microendoscopy," Opt. Express **15**(25), 16413–16423 (2007).

33. M. K. Quinn, T. C. Bubi, M. C. Pierce, M. K. Kayembe, D. Ramogola-Masire, and R. Richards-Kortum, "High-Resolution Microendoscopy for the Detection of Cervical Neoplasia in Low-Resource Settings," PLoS One **7**(9), e44924 (2012).

34. D. Shin, M. C. Pierce, A. M. Gillenwater, M. D. Williams, and R. R. Richards-Kortum, "A Fiber-Optic Fluorescence Microscope Using a Consumer-Grade Digital Camera for In Vivo Cellular Imaging," PLoS One **5**(6), e11218 (2010).

35. W. Zhong, J. P. Celli, I. Rizvi, Z. Mai, B. Q. Spring, S. H. Yun, and T. Hasan, "In vivo high-resolution fluorescence microendoscopy for ovarian cancer detection and treatment monitoring," Br. J. Cancer **101**(12), 2015–2022 (2009).

36. H. Wang, N. Zhang, and S. Zuo, "Low-cost and highly flexible intraoperative endomicroscopy system for cellular imaging," Appl. Opt. **57**(7), 1554–1561 (2018).

37. T. Kobayashi, T. Katagiri, and Y. Matsuura, "Fabrication of bundle-structured tube-leaky optical fibers for infrared thermal imaging," in *Optical Fibers and Sensors for Medical Diagnostics and Treatment Applications XVII* (SPIE, 2017), 100580X.

38. Y. Matsuura and K. Naito, "Flexible hollow optical fiber bundle for infrared thermal imaging," Biomed. Opt. Express **2**(1), 65–70 (2011).

39. E. Rave, D. Shemesh, and A. Katzir, "Thermal imaging through ordered bundles of infrared-transmitting silver-halide fibers," Appl. Phys. Lett. **76**(14), 1795–1797 (2000).

40. B. Zhang, C. Zhai, S. Qi, W. Guo, Z. Yang, A. Yang, X. Gai, Y. Yu, R. Wang, D. Tang, G. Tao, and B. Luther-Davies, "High-resolution chalcogenide fiber bundles for infrared imaging," Opt. Lett. **40**(19), 4384–4387 (2015).

41. M. S. Pochechuev, I. V. Fedotov, O. I. Ivashkina, M. A. Roshchina, D. V. Meshchankin, D. A. Sidorov-Biryukov, A. B. Fedotov, K. V. Anokhin, and A. M. Zheltikov, "Reconnectable fiberscopes for chronic in vivo deep-brain imaging," J. Biophotonics **11**(4), e201700106 (2018).

42. M. Yamane and Y. Asahara, *Glasses for Photonics* (Cambridge University Press, Cambridge, 2000).

43. J.-H. Han, J. Lee, and J. U. Kang, "Pixelation effect removal from fiber bundle probe based optical coherence tomography imaging," Opt. Express **18**(7), 7427–7439 (2010).

44. C.-Y. Lee and J.-H. Han, "Elimination of honeycomb patterns in fiber bundle imaging by a superimposition method," Opt. Lett. **38**(12), 2023–2025 (2013).

45. D. Kim, J. Moon, M. Kim, T. D. Yang, J. Kim, E. Chung, and W. Choi, "Toward a miniature endomicroscope: pixelation-free and diffraction-limited imaging through a fiber bundle," Opt. Lett. **39**(7), 1921–1924 (2014).

46. G. W. Cheon, J. Cha, and J. U. Kang, "Random transverse motion-induced spatial compounding for fiber bundle imaging," Opt. Lett. **39**(15), 4368–4371 (2014).

47. J. Cimek, R. Stępień, G. Stępniewski, B. Siwicki, P. Stafiej, M. Klimczak, D. Pysz, and R. Buczyński, "High contrast glasses for all-solid fibers fabrication," Opt. Mater. **62**, 159–163 (2016).

48. D. Pysz, I. Kujawa, R. Stępień, M. Klimczak, A. Filipkowski, M. Franczyk, L. Kociszewski, J. Buźniak, K. Haraśny, and R. Buczyński, "Stack and draw fabrication of soft glass microstructured fiber optics," Bull. Pol. Acad. Sci. Tech. Sci. **62**(4), 667–682 (2014).

49. R. Stepien, J. Cimek, D. Pysz, I. Kujawa, M. Klimczak, and R. Buczynski, "Soft glasses for photonic crystal fibers and microstructured optical components," Opt. Eng. **53**(7), 071815 (2014).

50. X. Chen, K. L. Reichenbach, and C. Xu, "Experimental and theoretical analysis of core-to-core coupling on fiber bundle imaging," Opt. Express **16**(26), 21598–21607 (2008).

51. K. Chung and K. Deisseroth, "CLARITY for mapping the nervous system," Nat. Methods **10**(6), 508–513 (2013).

52. J. B. Anders Bjarklev, Araceli Sanchez Bjarklev, *Photonic Crystal Fibres,* 1 ed. (Springer US, 2003).

53. Z. A. Steelman, S. Kim, E. T. Jelly, M. Crose, K. K. Chu, and A. Wax, "Comparison of imaging fiber bundles for coherence-domain imaging," Appl. Opt. **57**(6), 1455–1462 (2018).

54. M. C. Hudson, "Calculation of the Maximum Optical Coupling Efficiency into Multimode Optical Waveguides," Appl. Opt. **13**(5), 1029–1033 (1974).

55. U. A. Gamm, C. L. Hoy, F. van Leeuwen-van Zaane, H. J. Sterenborg, S. C. Kanick, D. J. Robinson, and A. Amelink, "Extraction of intrinsic fluorescence from single fiber fluorescence measurements on a turbid medium: experimental validation," Biomed. Opt. Express **5**(6), 1913–1925 (2014).

56. R. Paschotta, *Encyclopedia of Laser Physics and Technology,* 1st ed. (Wiley-VCH, 2008), p. 856.

57. J. Schaffer and H. Bauch, "Test preparation for microscopes," U.S. Patent 20040180384 (2004).